Nanograting-based compact VUV spectrometer and beam profiler for *in-situ* characterization of high-order harmonic generation light sources

Oleg Kornilov,[1] Russell Wilcox,[2] and Oliver Gessner[1]

[1] *Ultrafast X-ray Science Laboratory, Chemical Sciences Division,*

Lawrence Berkeley National Laboratory, Berkeley, CA 94720

[2] *Engineering Division, Lawrence Berkeley National Laboratory, Berkeley, CA 94720*

(Dated: July 9, 2010)

Abstract

A compact, versatile device for VUV beam characterization is presented. It combines the functionalities of a VUV spectrometer and a VUV beam profiler in one unit and is entirely supported by a standard DN200 CF flange. The spectrometer employs a silicon nitride transmission nanograting in combination with a micro-channel plate based imaging detector. This enables the simultaneous recording of wavelengths ranging from 10 nm to 80 nm with a resolution of 0.25 nm to 0.13 nm. Spatial beam profiles with diameters up to 10 mm are imaged with 0.1 mm resolution. The setup is equipped with an in-vacuum translation stage that allows for *in situ* switching between the spectrometer and beam profiler modes and for moving the setup out of the beam. The simple, robust design of the device is well suited for non-intrusive routine characterization of emerging laboratory- and accelerator-based VUV light sources. Operation of the device is demonstrated by characterizing the output of a femtosecond high-order harmonic generation light source.

PACS numbers: 07.60.Rd, 07.85.Nc, 42.79.Pw, 42.65.Ky, 42.60.Jf

I. INTRODUCTION

Novel VUV light sources are the tools of the trade of a fast growing scientific community that extends the field of ultrafast real-time studies into photon energy regimes beyond the realm of conventional femtosecond lasers [1, 2]. In particular laboratory-scale setups that employ the technique of high-order harmonic generation (HHG) driven by an intense infrared (IR) femtosecond laser allow for a new class of time-domain experiments using moderately intense femtosecond and even attosecond duration VUV light pulses. Prominent examples for this emerging field of ultrafast science are the direct determination of an atomic inner-shell hole lifetime [3], the real-time monitoring of unimolecular dissociation dynamics [4, 5], the observation of delayed photoemission from solids [6], the quantum state-resolved probing of aligned electron holes created by strong-field ionization [7] and the real-time observation of electron tunneling [8].

Despite the widespread application of HHG based VUV light sources in fundamental research, to the best of our knowledge no design has been reported for a compact, non-intrusive tool for *in-situ* characterization of two of the most important characteristics of a VUV light beam, the photon energy spectrum and the spatial beam profile. This is in stark contrast to the established field of ultrafast research in the IR/visible regime, which heavily relies on in-situ beam characterization using commercially available spectrometers and beam profilers. VUV spectrometers are of course ubiquitous in many research laboratories and designs have been reported that are specifically tailored toward the detection of HH's [9, 10]. In general, however, these spectrometers are designed and built to become a stationary part of the experiment, i.e. the recorded spectrum is the experimental result. This often leads to a layout that makes it difficult to use the spectrometer as a fast diagnostic for a VUV light beam that is used for different experiments, such as photoelectron or ion spectroscopy. Owing to the small ratio between the short wavelengths of VUV radiation and standard grating constants, the size of a VUV spectrometer is usually on the scale of ≈ 1 m, contributing a significant fraction to the overall laboratory footprint of the experiment. Mobile optics that permit to route the VUV beam either into the experiment or the spectrometer are often incompatible with the requirement for interferometric stability in experiments such as attosecond time-resolved spectroscopy.

Here, we present a highly sensitive VUV beam analyzer that combines the functionalities

2

of a spectrometer and a beam profiler in a single compact unit that can readily be implemented in most experimental setups. It employs a transmission nanograting in combination with a microchannel plate (MCP) based imaging detector. The entire unit is mounted on a standard DN200 CF vacuum flange; the in-vacuum dimensions are less than 200 mm x 200 mm x 100 mm (length x width x height). Wavelengths ranging from 10 nm to 80 nm are recorded simultaneously with a resolution that varies from 0.25 nm to 0.13 nm across the spectral range. Beam profiles with diameters up to 10 mm are imaged with 0.1 mm resolution. The sensitivity of the device is adjustable, the upper limit reaching the single photon counting regime. The large dynamic range in combination with a low background noise enables the characterization of a large variety of VUV light sources. All in-vacuum components are mounted on a remote-controlled translation stage. Switching between the operating modes of the beam analyzer as well as the removal of the unit from the VUV beam path is completed within minutes. The design removes any impact of the beam analysis on the alignment of experimental components and effectively de-couples the precision of the stage motion from the spectrometer resolution.

The functionality of the VUV spectrometer and beam profiler is demonstrated by characterizing the output of a HHG light source that is based on a loosely focused IR driving pulse and a differentially pumped gas cell. An elliptical VUV beam profile is observed. Numerical simulations of coherent beam propagation show that it is the result of a commonly used astigmatic driver focusing geometry. Adjusting the temporal chirp of the driving IR laser leads to significant changes in the HH spectrum including splitting of HH peaks. The spectral structures may be due to interference effects in the single atom response to chirped driver pulses as recently described by Liu and co-workers [11].

II.   DESIGN

A photograph of the device is shown in Fig. 1, the main components are sketched in Fig. 2. All elements of the spectrometer and beam profiler except for the digital camera are mounted on a standard optical breadboard. The breadboard is attached to a linear translation stage with 50 mm maximum travel distance (Newport 436). For increased vacuum compatibility, the stage is disassembled, anodized surface layers are removed and the crossed roller bearing lubricant is replaced by a vacuum-compatible grease (Apiezon L). The entire
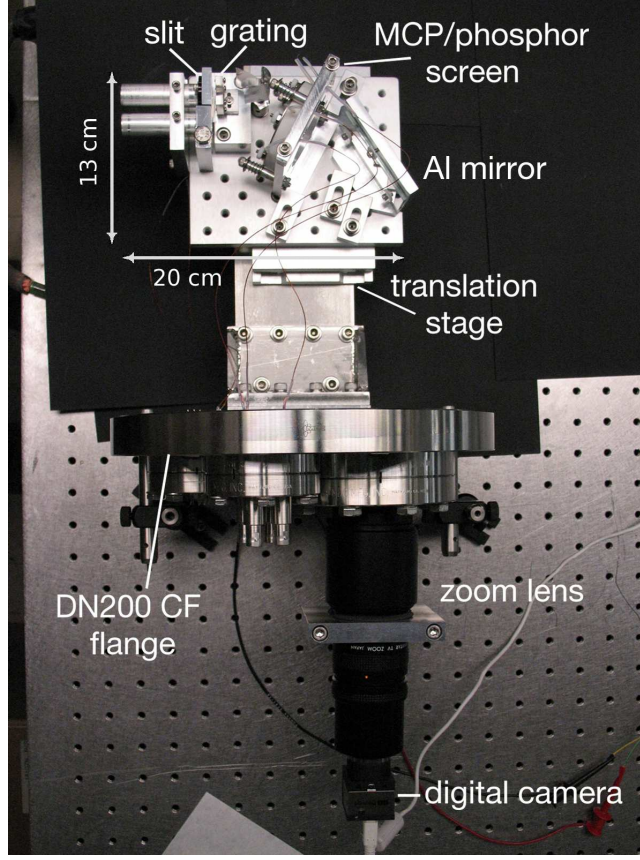
3

FIG. 1: VUV spectrometer and beam profiler device mounted on a DN200 CF flange.

setup is mounted on a standard DN200 CF vacuum flange, facilitating quick integration of the device into existing experimental setups. The stage position is controlled by a high vacuum compatible piezo-actuator (Newport Picomotor 8303-V) that facilitates remote in-vacuum switching between spectrometer (Fig. 2, position (a)) and beam profiler (Fig. 2, position (b)) modes and clearing the VUV beam axis by ~ 10 mm for experiments that require light downstream from the spectrometer. In spectrometer and beam profiler modes, the VUV beam enters the setup through 30 mm long tubes with 10 mm inner diameter in order to limit the amount of background light in the system.

In spectrometer mode, the beam passes through the 50 μm wide entrance slit and is incident on the transmission nanograting at an angle of 0° (normal to the grating plane). The SiN transmission grating (nm^2 LLC) used in this setup was developed by T. Savas and H. Smith [12, 13]. The grating is composed of free-standing 44 nm wide bars with a 100 nm periodicity, leaving 56 nm wide spaces between the bars. The bars are developed from a
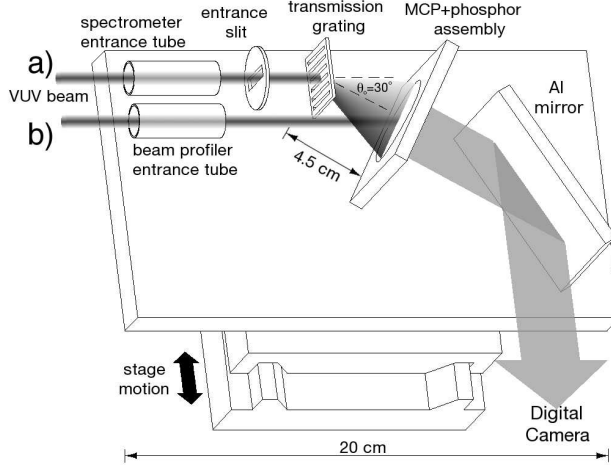
FIG. 2: In spectrometer mode (a), the VUV beam passes through the entrance tube, the 50 μm wide entrance slit and is dispersed by the transmission grating. The diffraction pattern is detected by the MCP-phosphor screen assembly and imaged onto a digital camera through a DN63 viewport by means of an Al mirror. In beam profiler mode (b), the VUV beam passes through an entrance tube and is directly incident on the MCP detector. The direction of motion of the translation stage is indicated by the double arrow.

200 nm thick SiN membrane by achromatic lithography [12, 13]. For improved mechanical stability of the grating, the vertical bars are intercepted by horizontal support structures spaced by approximately 1.5 μm. The small period of the grating facilitates a compact spectrometer design with a resolution of 0.25 nm to 0.13 nm at wavelengths of 10 nm and 80 nm respectively.

In beam profiler mode, the VUV beam is incident on the imaging detector at angles of 30° horizontally and 0° vertically. To correct for the effect of this geometry on the beam profile, the detector image is scaled horizontally by a factor $\frac{\sqrt{3}}{2}$ during the analysis.

The imaging detector (Beam Imaging Solutions) consists of two resistance-matched imaging quality MCPs (Burle Photonis) in Chevron configuration combined with an aluminized P-20 phosphor screen. The active area of the round detector is 40 mm in diameter. The detector is attached to the optical breadboard with a home-built mount equipped with a polytetrafluoroethylene (PTFE)-lined cable clamp to minimize stress on the high-voltage contacts during motion. In order to minimize variations of detection efficiency across the imaging detector in the dispersive plane due to differences in photon incidence angles, the
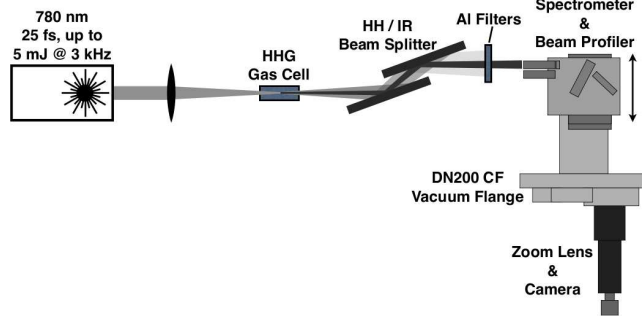
FIG. 3: Experimental setup for high-order harmonic generation and analysis [14].

MCP stack is aligned such that the channels are tilted in the vertical plane only. Uncoated, rimless 1.5 mm thick MCPs with 25 μm nominal pore size and 8° bias angle convert incident photons into electron bunches that are accelerated onto the phosphor screen.

The front of the MCP assembly is mounted at a distance of $L = 45$ mm from the center of the diffraction grating. The detector surface normal is tilted relative to the VUV beam propagation direction by $\theta_0 = 30°$ (Fig. 2). The fluorescence of the phosphor screen is imaged through a DN63 CF vacuum viewport onto a zoom-lens equipped digital camera by means of an enhanced Al utility mirror (Newport). In the present setup, the 1280x1024 pixels CMOS camera (Edmund Optics) is used in integration mode. The zoom-lens is adjusted to image a 44 mm wide area onto the camera corresponding to a pixel limited resolution of 35 μm. With single-shot detection and centroiding analysis, the uncertainty due to electron bunch size can be reduced down to the MCP pore size of approximately 25 μm.

Performance of the spectrometer and beam profiler is demonstrated by characterizing a VUV beam produced by high-order harmonic generation (HHG) in Ar and Kr (Fig. 3) [1, 2, 14–18]. An intense femtosecond infrared (IR) laser beam is generated by routing the output of a mode-locked Ti:sapphire laser through a cryogenically cooled two-stage amplifier system (Red Dragon, KM Laboratories). The IR beam with a diameter of 20 mm is focused by a concave mirror with 2 m nominal focal length into a target cell filled with noble gases at pressures of several mbar. The cell is terminated by 50 μm thick Ni foils on both ends. The IR beam drills a path through these foils within a fraction of a second. A high throughput turbomolecular pump (Shimadzu TMP 3203LM) maintains a pressure difference of about 6 orders of magnitude between the gas cell and the surrounding vacuum chamber. The strong IR field (up to 10^{15} W/cm^2) ionizes the target gas. Field-driven electron-ion recollision and

6

recombination leads to emission of radiation at frequencies equal to odd integer multiples of the fundamental laser frequency. The maximum achievable photon energy depends on the maximum peak power of the focused laser pulse and the ionization potential of the gas [1, 2, 16–18]. HH light emerges from the cell collinearly with the driver laser beam and is separated from the co-propagating IR by two reflections from superpolished pure silicon mirrors under Brewster angle geometry for the IR beam, and subsequent passage through an aluminum filter. To avoid detector saturation, a set of aluminum filters of various thicknesses (100 nm - 7 μm) are mounted on an in-vacuum manipulator that is separate from the spectrometer assembly.

III. DIFFRACTION FROM A TRANSMISSION NANOGRATING

The compact design of the spectrometer voids the application of small angle approximations and leads to geometry-induced variations of the spectral sensitivity. In the following, equations are derived that are needed to extract relative spectral intensities from the experimental images. In addition, they are used for the precise determination of the detector position with respect to the diffraction grating, as described in the next section.

For a normal incidence geometry, the diffraction angle θ for the nth diffraction order is given by:

$$\sin \theta = n\frac{\lambda}{d}, \tag{1}$$

where λ is the wavelength of the incident light and d=100 nm is the period of the grating. A typical diffraction pattern is shown in Fig. 4a. It is recorded using a 4 μm thick Al filter and an image integration time of 30 s. Potential differences of 1450 V across the MCP stack and 2350 V between the stack and the phosphor screen are applied. The VUV beam is generated using 25 fs duration IR driving pulses (785 nm) with 3.6 mJ pulse energy. The HHG gas cell is filled with Ar at a stagnation pressure of 5.3 mbar. The vertical lines in the image correspond to the signal from individual harmonics separated by 3.2 eV (twice the 1.6 eV photon energy of the IR driving laser).

The individual harmonic traces seen in Fig. 4a are vertically elongated. Their detailed structure is better resolved in Fig. 5a, which is recorded using a 100 nm thick Al filter. The central part of the image is strongly saturated, the upper and lower parts display a series of vertically displaced maxima for each harmonic with a characteristic crescent shape. This
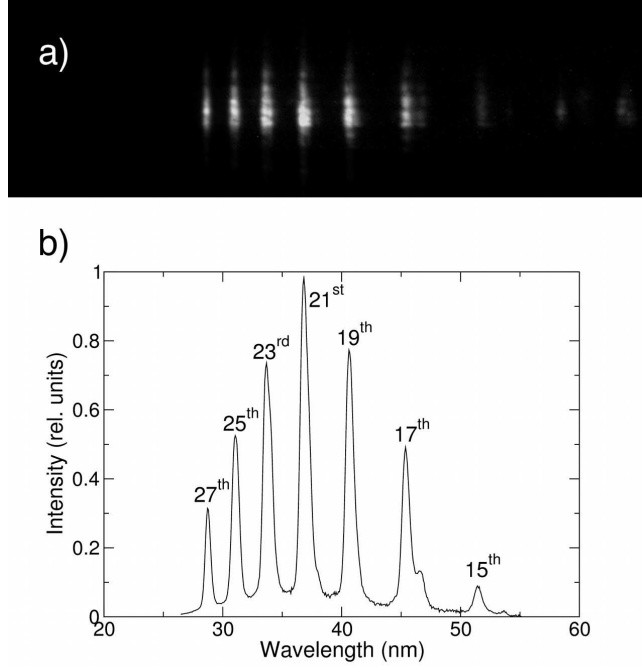
FIG. 4: (a) Image of the diffraction pattern of a femtosecond VUV light beam recorded using a 4 μm thick aluminum filter. (b) Spectrum extracted from (a) by analysis of the 2D diffraction pattern as described in the text.

pattern is caused by diffraction of the VUV light on the periodic support structure of the grating as discussed by Wilhein and co-workers [19]. The period of the support structure is about 1.5 μm and thus the first order diffraction angle at a wavelength of 50 nm is 1.9° corresponding to a vertical displacement of approximately 1.5 mm on the detector screen.

To understand the crescent shape of the diffraction patterns of individual harmonics, it is necessary to consider diffraction in two dimensions (Fig. 6). Let $\vec{k}$ be the wave vector of the diffracted light and k_x, k_y, k_z its components along the three cartesian axes: the z axis is pointing along the beam direction, the y axis is pointing vertically along the grating bars and the x axis is pointing horizontally to the right when looking along the z axis. Due to energy conservation, the length of the wave vector remains unchanged upon diffraction. Diffraction in two dimensions can be described by a change in the wavevector direction in the horizontal and vertical planes equal to integer multiples of the reciprocal periods of the
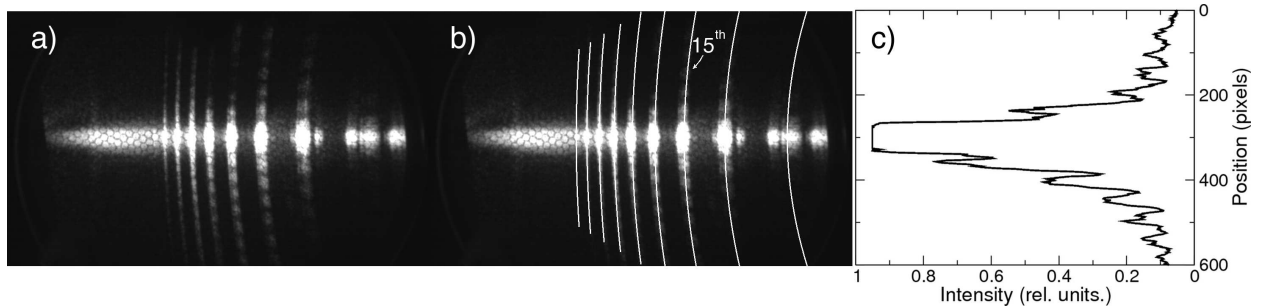
FIG. 5: (a) Diffraction image of the HHG beam generated using laser parameters similar to Fig. 4 and recorded using a 100 nm thick aluminum filter. In the central region the spectrum is saturated. (b) The same image as in (a) with superimposed vertical diffraction lines calculated using the method described in the text. (c) Vertical diffraction pattern of the 15$^{\text{th}}$ harmonic extracted from (b).
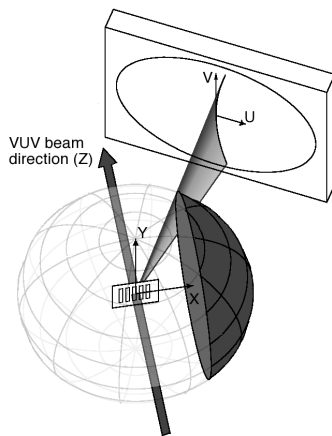

FIG. 6: Geometry of the VUV beam diffraction.

grating and the support structure:

$$\Delta \vec{k} = n_x \vec{e_x} \frac{2\pi}{d_x} + n_y \vec{e_y} \frac{2\pi}{d_y}. \tag{2}$$

Here, $\vec{e_x}$ and $\vec{e_y}$ are the unit vectors in the corresponding directions, n_x and n_y are the diffraction orders, and d_x and d_y are the periods of the grating and the support structure, respectively. For gratings with open aperture ratios close to 50%, second order diffraction maxima are strongly suppressed. Therefore, only the case of $n_x = 1$ will be discussed in the following. It is straightforward to generalize the results to higher diffraction orders.

9

By definition, the components of the incident wavevector along the x and y axis are equal to zero and thus the diffracted beam components are equal to the corresponding projections of $\Delta\vec{k}$. The third component k_z is determined by energy conservation:

$$k_z^2 = k^2 - k_x^2 - k_y^2. \tag{3}$$

The diffraction angle in the horizontal plane is given by the ratio of the two wavevector projections:

$$\tan(\theta_x) = \frac{k_x}{k_z}. \tag{4}$$

In the case of additional vertical diffraction, increasing values of k_y lead to a decrease of k_z according to (3) and thus to larger values of the horizontal diffraction angle θ_x in (4). As shown in Fig. 6, the resulting curvature of the first order diffraction maximum of a single harmonic is given by the curvature of a section of a sphere of radius k. The two-dimensional diffraction patterns can be calculated by intersecting the directions of the diffraction maxima with the detector plane positioned at a distance L from the center of the grating with the angle θ_0 between the surface normal and the VUV beam direction:

$$x = \frac{Lk_x}{k_x \sin\theta_0 + k_z \cos\theta_0}$$
$$y = \frac{k_y}{k_x}x \tag{5}$$

To analyze the spectra recorded by the camera, it is more convenient to transform these equations into a coordinate system in the detector plane. Let u be the horizontal coordinate of the image recorded by the camera and v be the vertical coordinate (Fig. 6). The origin of the u, v coordinate system is the normal projection of the grating center on the detector plane. Since the back of the detector is imaged onto the camera by a mirror, the direction of u in the camera image is the same as in the detector plane, it points toward increasing diffraction angles.

$$u = (x - L\sin\theta_0)/\cos\theta_0$$
$$v = y \tag{6}$$

For diffraction in the horizontal plane ($y = v = 0$), the wavelength of the detected radiation can be expressed as a function of the pixel position u in screen coordinates:

$$\lambda = d \cdot \sin\left(atan\left(\frac{u - u_0}{A}\right) + \theta_0\right). \tag{7}$$

Here, u_0 is the position of the origin of the u, v coordinate system, $\theta_0 = 30°$ is the angle between the detector plane normal and the VUV beam direction, $d = 100$ nm is the period of the grating and the constant A depends on the magnification of the imaging system and the distance between the grating and the detector plane ($L = 45$ mm).

Equations (2)-(6) are employed to derive the VUV spectrum from the two-dimensional detector image. They are also used to calibrate the detector angle θ_0 and the distance L between the MCP and the grating by analyzing a spectrum containing two or more known wavelengths. This calibration is usually more precise than the determination of θ_0 and L with standard measuring techniques since mechanical precision tools such as calipers and angle protractors are hard to use without damaging the fragile components. The supplementary material for this publication [20] contains computer programs, written for GNU Octave scientific package, that can be used for parameter calibration and generation of VUV spectra as described above. The crescent diffraction patterns are shown in Fig. 5b by white lines. Integration of the image in Fig. 4a along these crescent lines results in the spectrum shown in Fig. 4b.

The analysis of the diffraction pattern described above is used to estimate the spectrometer resolution. The width of the entrance slit of 50 μm contributes a wavelength uncertainty of approximately 0.08 nm at a wavelength of 50 nm. The resolution is further affected by the spot size of the electron bunch of about 70μm generated by the MCP assembly [21] and by the resolution of the digital camera used for imaging. The combined wavelength uncertainty is estimated to be $\Delta\lambda = 0.24$ nm ($\Delta E = 120 meV$) at a wavelength of $\lambda = 50$ nm (24.8 eV) corresponding to a resolving power of $\lambda/\Delta\lambda \approx 210$. The spectral resolution varies across the detector from $\Delta\lambda = 0.13$ nm ($\Delta E = 12$ meV) at the low-energy side ($\lambda = 80$ nm, $E = 15.5$ eV) to $\Delta\lambda = 0.25$ nm ($\Delta E = 1.6$ eV) at the high-energy side ($\lambda = 10$ nm, $E = 124$ eV).

IV.   INTENSITY CALIBRATION

To extract relative intensities from the recorded spectra, it is necessary to account for three factors that introduce a wavelength dependence in the spectrometer detection efficiency: i) the wavelength dependence of the MCP quantum detection efficiency (QDE), ii) the angular dependence of the QDE, and iii) the diffraction efficiency of the transmission
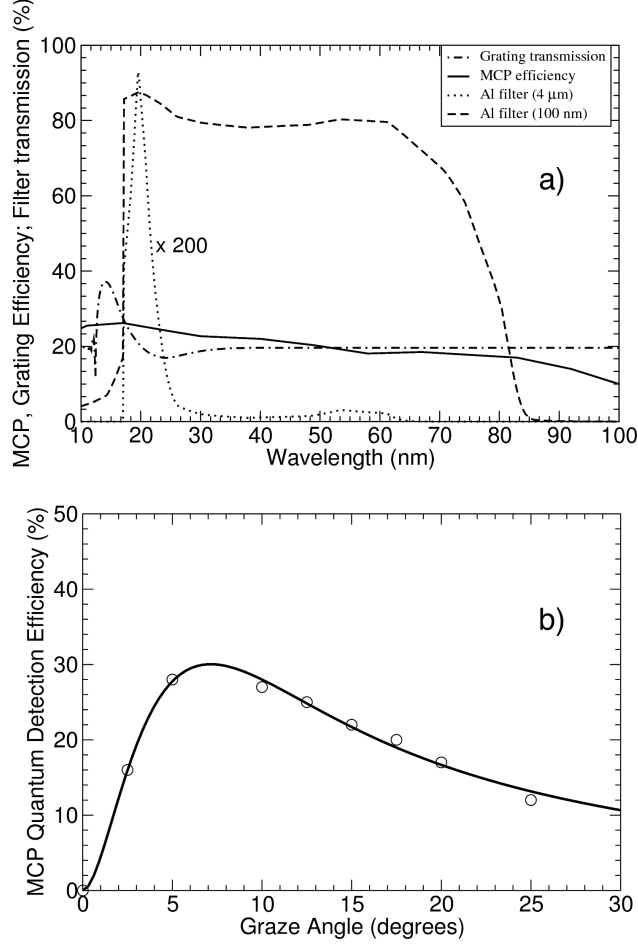
FIG. 7: (a) Wavelength dependence of the grating diffraction efficiency in the first order (dash-dotted) [22], MCP quantum detection efficiency (solid) [23] and transmission functions of a 100 nm (dashed) and a 4 μm (dotted, multiplied by 200) thick aluminum filter [22]. (b) Angular dependence of the MCP quantum detection efficiency. The experimental data (open circles) are taken from [23], the solid line is the result of a least square fit using the empirical Eq. (8).

grating.

The wavelength and angular dependence of MCP quantum detection efficiencies have been studied both experimentally [23–25] and theoretically [26–28]. For MCPs similar to those used in our imaging system, both angular and wavelength dependences of the QDEs are given by Siegmund and co-workers [23]. The wavelength dependence from Fig. 2 of Ref. [23] is plotted in Fig. 7a as a solid line. The measured QDE angular dependence from Fig. 3 of Ref. [23] covers a range of graze angles $\phi = 0° - 25°$. The angular dependence of the

QDE at larger graze angles is proportional to $\cot(\phi)$ [26, 27]. An empirical fit function with this asymptotic dependence is used to calculate the QDE angular dependence $Q(\phi)$ across the entire range of incidence angles $\phi = 0° - 40°$ of the spectrometer setup:

$$Q(\phi) = Q_0 \left(1 - e^{-\phi/\phi_m}\right)^3 \cdot \cot(\phi), \tag{8}$$

ϕ is the graze angle between the incident beam and the MCP pore axis. The constants $Q_0 = 0.062$ and $\phi_m = 0.066$ are determined by a least square fit. The experimental data of Ref. [23] together with a fit according to Eq. (8) are plotted in Fig. 7b. Using Eqs. (2)-(6) and the efficiency data from Fig. 7, a two-dimensional calibration matrix is derived that assigns a total detection efficiency to every point on the detector. The calculation takes into account that the pores of the micro-channel plates are tilted vertically at an angle of $8°$.

The detector images are integrated along the diffraction pattern in the vertical dimension after correcting for angular and wavelength dependence of the QDE. Apart from these corrections it is only necessary to account for the first order diffraction efficiency in the horizontal dimension. This efficiency is calculated using the "X-ray interaction with matter" calculator of the Center for X-ray Optics (CXRO) at Lawrence Berkeley National Laboratory [22]. The grating efficiency curve is plotted in Fig. 7a as a dash-dotted line.

By normalizing the measured spectrum using the Al filter transmission curve, the spectrum of the HHG source upstream from the filter is derived. The filter transmission curves are calculated using the "X-ray interaction with matter" calculator of the Center for X-ray Optics [22]. The transmission curves for the 100 nm and 4 μ thick Al filters are shown in Fig. 7a as dashed and dotted lines, respectively.

V. CHARACTERIZATION OF A HHG BASED FEMTOSECOND VUV LIGHT SOURCE

The performance of the spectrometer and beam profiler is demonstrated by probing the spatial beam profile of a HHG based VUV light source and the dependence of the VUV spectrum on the temporal chirp of the IR driver pulse. A typical VUV beam profile is shown in Fig. 8. The honeycomb structure in the image is a result of the MCP channel packing geometry. The beam profile has an elliptical, vertically elongated shape. The side panels in Fig. 8 show the intensity distributions along the vertical and horizontal axes,
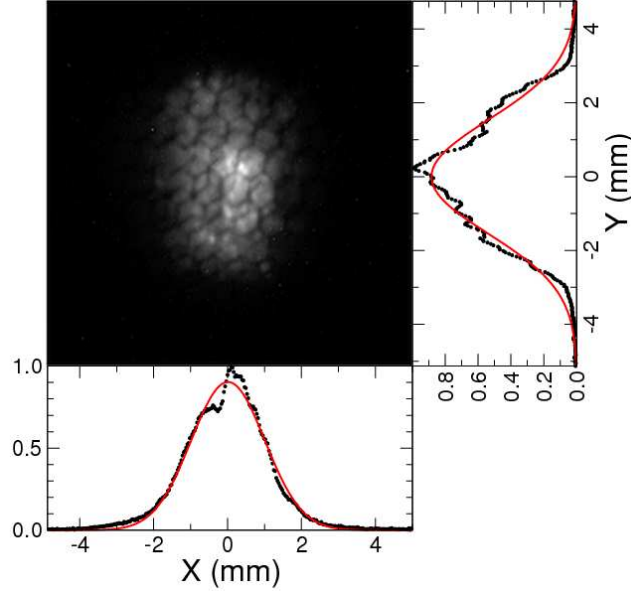
13

FIG. 8: The spatial profile of the HH beam generated at conditions similar to the ones in Fig. 4. The hexagonal shapes are due to the MCP channel packing structure. The profiles in the side and bottom panels are derived by integrating the image along the X and Y axis, respectively. Fits to Gaussian functions (solid lines) are used to derive the beam dimensions (FWHM) of 2.5 mm x 4.0 mm (X x Y).

derived by integrating the two-dimensional beam profile along the horizontal and vertical axis, respectively. Fits to Gaussian distribution functions (smooth solid lines) lead to beam full-widths-at-half-maximum (FWHM) of 4.0 mm (vertically) and 2.5 mm (horizontally). The beam analyzer is positioned 2.40 m away from the HHG source. Correspondingly, the far-field divergence angle Θ_{HH} is on the order of Θ_{HH}=1-2 mrad. The IR beam focusing geometry corresponds to a far-field divergence of Θ_{IR}=10 mrad. A Gaussian beam description requires the beam divergence for a fixed beam waist to scale exactly with the wavelength, corresponding to a divergence ratio of 15 to 27 between the fundamental IR driving beam and the 15th to 27th harmonic. However, the beam waist for HH is smaller than for the IR driver since only the regions of highest intensities contribute to HHG. This reduction of the HH source volume compared to the focal size of the IR driver leads to an increased divergence of the HH beam as observed.

The elliptical shape of the HH beam profile is the result of an astigmatic geom-

14

etry. The IR beam is focused by a concave mirror with a 4 m radius that reflects the driver pulse at incidence angles of 16 mrad (horizontally) and 0 mrad (vertically). The IR beam passes through the meridional and the sagittal focus before it enters the gas cell, the foci being placed at a distance of $\approx 2-4$ mm from the cell entrance aperture. This upstream focusing geometry is known to yield the best HHG efficiency [29, 30]. The geometry implies that HHs are generated closer to the sagittal than the meridional focus, where the astigmatic beam is horizontally elongated [31]. The HH source volume is therefore more strongly confined in the vertical than in the horizontal direction. Gaussian beam propagation results in a larger far-field divergence in the vertical direction and a smaller in the horizontal direction, leading to the observed elliptical beam profile.

The qualitative discussion of the beam profile is confirmed by the results of a numerical beam propagation simulation, illustrated in Fig. 9. Images (a) and (b) show intensity distributions of a simulated astigmatic beam close to the sagittal focus (a) and in the far field (b). The beam is simulated by introducing an astigmatic phase to a flat field Gaussian beam using a second order Zernike polynomial [32] and propagating the focused beam through the focal region using the LightPipes software package [33]. The far field intensity distribution is round as expected, because the larger divergence of the beam in the vertical plane after the focus is compensated by the astigmatic phase distribution. A HH beam is simulated by keeping the phase profile of the IR beam and raising the beam intensity to the 5th power [16]. This procedure reflects the correspondence between the spatial phase profile of the IR beam and the HH beam and accounts for the non-linear interaction leading to HH generation, which is expected to scale approximately with the 5th power of the driving IR intensity [16]. The sagittal focus profile of this beam is shown in Fig. 9c. After propagating the same distance as the beam in Fig. 9a,b, the simulated HH beam emerges with a vertically elongated shape (Fig. 9d) as is observed in the experiment.

This example demonstrates that the VUV beam profiler provides detailed information on the HHG source conditions and the HH beam propagation. This information is vital for the design of experiments that employ this novel class of light sources and for establishing reproducible light source conditions in day-to-day operations.

Operation of the spectrometer is demonstrated by recording a series of HH spectra generated by driving laser pulses with varying spectral chirps (Fig. 10). The chirp is modified by adjusting the position of one of the gratings in the compressor stage of the chirped-pulse
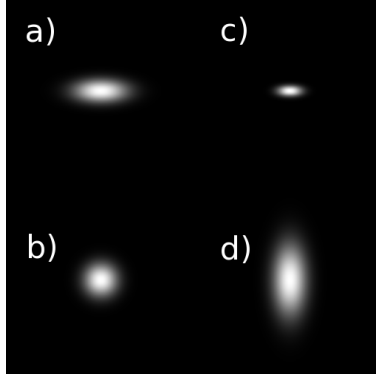
FIG. 9: Simulated effect of the astigmatic driver beam geometry on the HH beam due to the non-linear nature of HHG. Astigmatic driver beam intensity profiles are shown for the sagittal focus plane (a) and for the far field (b). Raising the intensity profile (a) to the 5th power (c) leads to an elliptical far field intensity distribution (d).
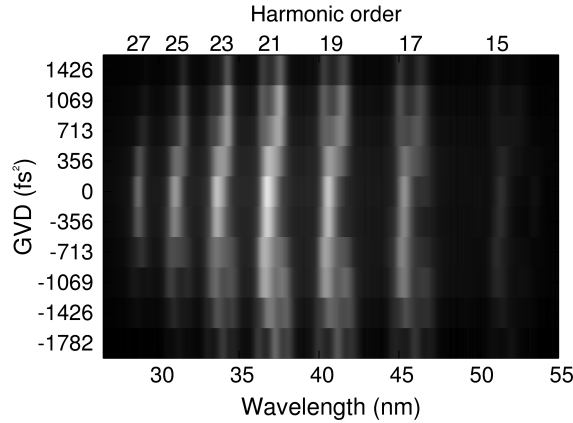

FIG. 10: HH spectra of the VUV beam generated at the same conditions as in Fig. 4, but for a variety of temporal chirps of the laser amplifier. The chirps are indicated on the vertical axis in terms of induced group velocity dispersion (GVD).

laser amplifier system, while keeping the pulse energy constant. The HH spectrum is changing significantly as the spectral chirp is varied. The shapes of individual peaks are changing from a three peak structure at large negative chirps to a single intense peak at near-zero chirps. For large positive chirps, the harmonic peaks are split again, exhibiting double-peak structures.

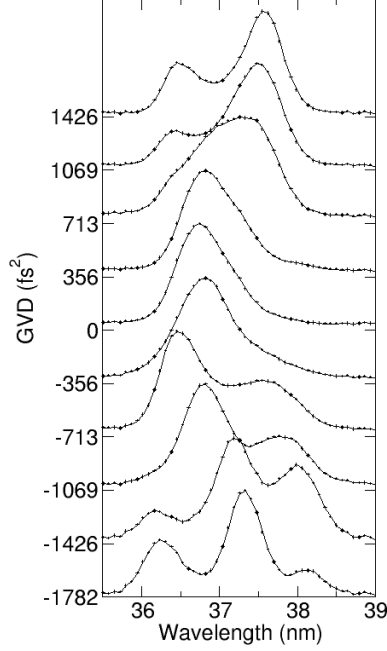A detailed picture of the driver chirp dependence of the HH spectrum can be seen in Fig.

FIG. 11: Spectral shape of the 21st harmonic as a function of GVD. The spectra are normalized to equal maximum intensity. The values and tick marks at the ordinate indicate the GVD for the corresponding spectra and the baseline positions.

11, which shows a waterfall representation of the data of Fig. 10 for the wavelength range of the 21st harmonic. The solid circles correspond to the camera pixels covered by the 21st harmonic and the group velocity dispersion (GVD) values are given on the left next to the base lines of the corresponding spectra. To guide the eye, the circles are connected by lines. Fig. 11 demonstrates that spectral features spaced by less than a nanometer can easily be resolved by the spectrometer. In fact, the shapes of the peaks are not determined by the spectrometer resolution but by the HH generation conditions. In all spectra the separation of features ranges from 1.0 to 1.3 nm.

It is known that variation of the spectral chirp of the driving laser pulse leads to spectral shifts and broadening of individual HH peaks [34]. The relation between HHG and the fundamental pulse chirp has previously been studied by several groups [30, 34–37]. These works mostly concentrate on the positions of the HH peaks and their width but do not discuss the splitting, even though it is observed experimentally [37] and appears in theoretical calculations of the single-atom response in HHG (Fig. 3 of Ref. [34]).

Recently, the structure of HH spectra has been theoretically analyzed by Liu and co-

workers [11]. Their calculations predict that interference effects between several quantum paths lead to a strong dependence of the HH spectrum on the spectral chirp of the IR driver pulse including the splitting of single harmonic peaks. It is shown that HHG involves contributions from several electron recollisions including short and long trajectories as well as second, third and higher order recollisions that occur when the electron does not recombine on the first passage of the core. The spectrum of HH radiation is determined by constructive interference of photons produced during all half-cycles of the femtosecond driver pulse that have sufficient intensity to generate photons of a certain energy. In the case of zero driver pulse chirp, contributions from similar trajectories of all consecutive half-cycles have equal phase shifts and thus the phase-matching is achieved for exact odd harmonics of the fundamental frequency of the driver pulse.

For chirped driver pulses the phase shifts gradually change from half-cycle to half-cycle. This induces interferences between contributions from different trajectories and leads to modulations in the HH spectra similar to those shown in Fig. 10, 11. Detailed calculations beyond the scope of this paper are needed for a quantitative comparison of theory and experiment.

VI. SUMMARY

A compact device is presented, that allows for fast, non-intrusive *in-situ* characterization of the photon energy spectrum and the spatial beam profile of laboratory-scale VUV light sources. The entire unit is mounted on a standard DN200 CF vacuum flange. The in-vacuum size of the device is less than 200 mm x 200 mm x 100 mm. Performance of the apparatus is demonstrated by analyzing the beam profile and the photon energy spectrum of a femtosecond high-order harmonic generation light source. An astigmatic focusing geometry of the IR driver pulse results in an elliptical VUV beam profile in agreement with numerical simulations of coherent beam propagation effects. Strong dependence of the VUV spectrum on the spectral chirp of the IR driver is demonstrated. The observed splitting of peaks in the high harmonic spectrum is in qualitative agreement with recent theoretical predictions that ascribe variations of the VUV spectrum to quantum interferences between different electron trajectories in the strong-field driven high-order harmonic generation process.

Acknowledgments

---

[1] T. Pfeifer, C. Spielmann, and G. Gerber, Rep. Prog. Phys. **69**, 443 (2006).

[2] T. Brabec and F. Krausz, Rev. Mod. Phys. **72**, 545 (2000).

[3] M. Drescher et al., Nature **419**, 803 (2002).

[4] L. Nugent-Glandorf et al., Phys. Rev. Lett. **87**, 193002 (2001).

[5] E. Gagnon et al., Science **317**, 1374 (2007).

[6] A. L. Cavalieri et al., Nature **449**, 1029 (2007).

[7] Z. H. Loh et al., Phys. Rev. Lett. **98**, 143601 (2007).

[8] M. Uiberacker et al., Nature **446**, 627 (2007).

[9] L. Poletto, S. Bonora, M. Pascolini, and P. Villoresi, Rev. Sci. Instr. **75**, 4413 (2004).

[10] L. Poletto et al., Rev. Sci. Instr. **80**, 123109 (2009).

[11] C. D. Liu et al., Opt. Express **17**, 10319 (2009).

[12] T. A. Savas, S. N. Shah, M. L. Schattenburg, J. M. Carter, and H. I. Smith, J. Vac. Sci. Technol. B **13**, 2732 (1995).

[13] T. A. Savas, M. L. Schattenburg, J. M. Carter, and H. I. Smith, J. Vac. Sci. Technol. B **14**, 4167 (1996).

[14] O. Kornilov et al., J. Phys. Chem. A **114**, 1437 (2009).

[15] E. Takahashi, Y. Nabekawa, T. Otsuka, M. Obara, and K. Midorikawa, Phys. Rev. A **66**, 021802R (2002).

[16] J. L. Krause, K. J. Schafer, and K. C. Kulander, Phys. Rev. Lett. **68**, 3535 (1992).

[17] P. B. Corkum, Phys. Rev. Lett. **71**, 1994 (1993).

[18] P. Salieres, A. L'Huillier, and M. Lewenstein, Phys. Rev. Lett. **74**, 3776 (1995).

[19] T. Wilhein et al., Rev. Sci. Instr. **70**, 1694 (1999).

[20] See supplementary material at [URL] for compter programs (GNU Octave) used for calibration and generation of the VUV spectra. .

[21] J. Bialkowski et al., Nucl. Instr. Method. **386**, 280 (1997).

[22] B. L. Henke, E. M. Gullikson, and J. C. Davis, Atom. Data Nucl. Data **54**, 181 (1993).

[23] O. Siegmund, J. Vallerga, and A. Tremsin, Proc. SPIE Int. Soc. Opt. Eng. **5898**, 58980H (2005).

[24] R. Hemphill, J. Edelstein, and D. Rogers, Appl. Optics **36**, 1421 (1997).

[25] O. H. W. Siegmund, E. Everman, J. V. Vallerga, J. Sokolowski, and M. Lampton, Appl. Optics **26**, 3607 (1987).

[26] G. W. Fraser, Nucl. Instr. Method. **195**, 523 (1982).

[27] O. L. Landen et al., Rev. Sci. Instr. **72**, 709 (2001).

[28] G. A. Rochau et al., Rev. Sci. Instr. **77**, 10E323 (2006).

[29] P. Salieres et al., Science **292**, 902 (2001).

[30] H. T. Kim et al., J. Phys. B-At. Mol. Opt. **37**, 1141 (2004).

[31] E. Hecht, *Optics (4th Edition)*, Addison Wesley, 4 edition, 2001.

[32] M. Born and E. Wolf, *Principles of Optics*, Cambridge University Press, 1998.

[33] G. Vdovin, H. van Brug, and F. van Goor, Proc. SPIE **3190**, 82 (1997).

[34] J. Zhou, J. Peatross, M. M. Murnane, and H. C. Kapteyn, Phys. Rev. Lett. **76**, 752 (1996).

[35] J. J. Carrera and S. I. Chu, Phys. Rev. A **75**, 033807 (2007).

[36] Z. Chang et al., Phys. Rev. A **58**, R30 (1998).

[37] D. G. Lee, J. H. Kim, K. H. Hong, and C. H. Nam, Phys. Rev. Lett. **87**, 243902 (2001).